

Cite this: *J. Mater. Chem. A*, 2019, 7, 4019

Giant enhancements in electronic transport and photoelectric properties of bismuth oxysulfide by pressure-driven 2D–3D structural reconstruction†

Ganghua Zhang,^{*ab} Qian Zhang,^a Qingyang Hu,^{ID a} Bihan Wang^a and Wenge Yang^{ID *a}HPSTAR
719-2019

Layered bismuth oxychalcogenides have been considered exciting material systems with potential applications in superconductivity and thermoelectricity, but their optoelectronic properties still require greater diligence. The pressure-driven 2D–3D structural reconstruction is an efficient strategy to *in situ* tune the electronic configuration of functional materials, and yet has remained a challenge for both fundamental studies and technological applications. Here, we present the pressure-driven buckling effects of the layered bismuth oxysulfide $\text{Bi}_9\text{O}_{7.5}\text{S}_6$ on a 3D network structure. Although no crystallographic symmetry change was observed up to 58.1 GPa, the layer and bonding distances between and within BiO and BiS layer changed dramatically, which drives the enhancements of electric conductivity by 6 orders of magnitude, increasing the photocurrent by 4 orders of magnitude, and significant narrowing down of band gap from 1.34 eV to 0.45 eV. These findings may open a new avenue for discovering and designing high-efficiency photodetectors and energy-harvesting materials.

Received 21st November 2018
Accepted 20th January 2019

DOI: 10.1039/c8ta11168e

rsc.li/materials-a

1. Introduction

Layered bismuth oxychalcogenides have attracted enormous scientific and engineering interest due to their anisotropic crystal and electronic structures with intriguing physical properties, such as superconductivity,^{1–3} thermoelectricity,^{4,5} ultra-high electron mobility and quantum oscillations.^{6,7} In contrast to the extensively studied superconductive and thermoelectric properties, few efforts have been devoted to their photoelectric performance, in spite of the fact that many chalcogenides have been considered as the potential candidates for power generation as well as solar energy conversion, such as $\text{Cu}(\text{In}_x\text{Ga}_{1-x})\text{Se}_2$ (CIGS),^{8,9} $\text{Cu}_2\text{ZnSnS}_4$ (CZTS)¹⁰ and CdTe .¹¹ Recently, in view of the suitable band gap and rapid photoelectric response, several layered bismuth oxychalcogenides $\text{Bi}_2\text{O}_2\text{Se}$,⁷ $\text{Bi}_2\text{O}_2\text{S}$ ¹² and $\text{Bi}_9\text{O}_{7.5}\text{S}_6$ (ref. 13) have been reported as promising light-absorbing materials for solar cell applications. However, their photocurrents are much lower than that of CIGS, CZTS and CdS ; therefore, no further investigation has been done on promoting their photoelectric performances to date. Furthermore, theoretical studies have assessed the use of BiOCuS for photovoltaic

applications with a high conversion efficiency of 18.8%.¹⁴ Due to the environmental friendliness and structural stability, these new light-absorbing materials with enhanced photoelectric performances would, of course, be more desirable.

As a significant technique to tune the crystal structure and electronic configuration of functional materials,^{15–18} high pressure has been demonstrated as an efficient route to modify the photoelectric-related properties. For instance, the pressure-induced anomalous visible-light response has been studied in organometal halide perovskites.^{19,20} In those studies, improved optical and electronic properties have been observed in GaAs nanowires under external pressure,²¹ and enhanced ferroelectric and photoelectric properties has been reported in multi-ferroic KBiFe_2O_5 .²² Among these, enhanced photocurrent can be achieved only in KBiFe_2O_5 , but the photocurrent density is still relatively low ($\sim 3.2 \mu\text{A cm}^{-2}$ for 5 mW cm^{-2} illumination at 30.5 GPa). Considerable modifications of the band gaps and conductivity of photoelectric materials could be realized by applied pressures, but no results with giant pressure-enhanced photoelectric performance have been reported so far. More interestingly, pressure-induced large emission enhancements have been achieved recently in several luminescent-related compounds, such as Cs_4PbBr_6 and CdSe ,^{23,24} providing a promising way for tuning bright-fluorescence imaging in response to an externally applied pressure. Thus, if significant enhancement in the photoelectric performance can be realized by pressure, hydrostatic pressure has immense potential for practical applications in photovoltaic devices as a switcher or controller due to the excellent stability and controllability.

^aCenter for High Pressure Science and Technology Advanced Research (HPSTAR), Shanghai 201203, P. R. China. E-mail: yangwg@hpstar.ac.cn; zhangjieess923@163.com

^bShanghai Key Laboratory of Engineering Materials Application and Evaluation, Shanghai Research Institute of Materials, Shanghai 200437, P. R. China

† Electronic supplementary information (ESI) available: Additional experimental results, Fig. S1–S10 and Table S1. See DOI: 10.1039/c8ta11168e

Commonly, layered structures show extremely large electronic anisotropy between in-plane and cross-plane conductivity, which are considerably sensitive to the external conditions.^{25,26} Moreover, due to the unusual variation of electronic states, the pressure-driven 2D–3D structural evolution in layered chalcogenides is quite different from the structural transition of other 3D materials.^{27,28} Thus, the desired electronic structure can be tuned by high pressure and promoted photoelectric performance can be expected in similar layered bismuth oxychalcogenides. In this study, we chose layered $\text{Bi}_9\text{O}_{7.5}\text{S}_6$, a newly synthesized two-dimensional (2D) oxysulfides with a suitable band gap (1.27 eV) and a rapid photoelectric response (~ 50 ms) for solar energy applications,¹³ as the candidate material for a step study toward this goal. The pressure-induced crystal structure evolutions, resistivity variations and the visible-light photoresponse of $\text{Bi}_9\text{O}_{7.5}\text{S}_6$ were studied by *in situ* X-ray diffraction (XRD), photoluminescence (PL) spectroscopy, electrical resistance (ER) and optoelectronic properties measurements. Giant enhancement of electrical conductivity and visible light response have been achieved by the pressure-induced 2D–3D structural transition, which suggests that the hydrostatic pressure technique is a powerful route to tune the structural, electronic and optoelectronic properties of the layered bismuth oxychalcogenides towards better photovoltaic performances.

2. Experimental

2.1 Sample preparation and characterizations

The detailed synthesis route for $\text{Bi}_9\text{O}_{7.5}\text{S}_6$ has been previously described.¹³ The sample was confirmed as pure $R\bar{3}m$ phase using a lab X-ray diffractometer (a Rigaku D/Max-2000 diffractometer with Cu K α radiation ($\lambda = 1.5418$ Å) at 40 kV, 100 mA and a graphite monochromator at the secondary beam). The morphology and composition of the pristine samples were investigated using a scanning electron microscopy (SEM) and energy dispersive spectrometer (EDS) with a FEI Quanta 200F microscope operating at 20 kV.

2.2 *In situ* high-pressure characterizations

A symmetrical DAC was employed to generate high pressure. A T-301 stainless steel gasket was pre-indented to 30 μm in thickness followed by laser-drilling the central part to form a 130 μm diameter hole to serve as the sample chamber. Pre-compressed $\text{Bi}_9\text{O}_{7.5}\text{S}_6$ powder pallet and three small ruby balls were loaded into the chamber. *In situ* high-pressure angle-dispersive X-ray diffraction (ADXRD) experiments were performed at the 16 BM-D station of the High-Pressure Collaborative Access Team (HPCAT) at the Advanced Photon Source (APS), Argonne National Laboratory (ANL). A focused monochromatic X-ray beam with about 5 μm in diameter (FWHM) and a wavelength of 0.3099 Å was used for the diffraction experiments. Neon was used as the pressure-transmitting medium (PTM), and the pressures were determined by the ruby fluorescence method.²⁹ The diffraction data were recorded on a MAR345 image plate and the two-dimensional (2D) patterns were integrated to one-dimensional (1D) patterns with the Fit2D program.³⁰ Rietveld refinements of the synchrotron

XRD patterns were performed with the general structure analysis system (GSAS) code.³¹ Transmission electron microscopy (TEM) was performed using a JSM-2100F/HR microscope at an accelerating voltage of 1600 V. The morphology and composition of the pristine samples were investigated using SEM and EDS with an FEI Quanta 200F microscope operating at 20 kV. High-pressure PL spectra were recorded on a Raman spectrometer at HPSTAR with an Nd-YAG 532 nm laser and an optical grating of 1200 g mm^{-1} . Electrical resistance measurements were conducted with a four-probe resistance test system in a diamond-anvil cell at pressures up to 58.1 GPa. In order to achieve the electrical insulation between the electrical leads and metal gasket, a cubic boron nitride (c-BN) layer was inserted between the steel gasket and diamond culet. Four platinum wires were arranged to contact the sample in the chamber for resistance measurements. A Keithley 6221 current source, 2182A nanovoltmeter, and 7001 switch system were used as the current supply, voltmeter, and voltage/current switcher, respectively. The resistance was determined by the Van der Pauw method.³² For the photocurrent measurement, a Zahner IM6 electrochemical workstation was used to record the I - t data by applying a constant voltage of 0.5 V. A fiber optic LED lamp with the max output ~ 100 mW was used as the irradiation source (~ 20 mW cm^{-2} on the sample).

2.3 Electronic structure calculation

In order to determine the band structures, the projector augmented wave (PAW) method³³ was used in the density-functional theory (DFT) calculations, which included the PBE version of the generalized gradient approximation (GGA) to describe the exchange correlation functional.³⁴ Here, the cutoff energy of plane wave was chosen at 350 eV. For structure optimizations, $6 \times 6 \times 6$ Monkhorst–Pack grids³⁵ were used for the primitive cell and $4 \times 4 \times 2$ k points for the conventional cell. The relaxation of geometry optimization was performed until the total energy changes within 10^{-6} eV per atom and the Hellmann–Feynman force on all atomic sites was less than 0.02 eV Å⁻¹.

3. Results and discussion

Hydrothermal method has been utilized to synthesize the $\text{Bi}_9\text{O}_{7.5}\text{S}_6$ crystals as was reported previously.¹³ The structure and morphology of the as-grown crystalline $\text{Bi}_9\text{O}_{7.5}\text{S}_6$ were characterized using XRD, SEM and EDS as given in Fig. S1.† From the *in situ* synchrotron X-ray diffraction measurements of $\text{Bi}_9\text{O}_{7.5}\text{S}_6$, all patterns are consistent with the hexagonal structure and no crystallographic symmetry change is observed up to 45.6 GPa and decompression at room temperature (see Fig. 1). Decompression of the sample shows that the shifts of all peaks are reversible. However, above 22.7 GPa, a 2D layered to 3D-type networked structural transition has been accomplished by the bonding of interlaminar Bi and S atoms upon the Rietveld refinements (Fig. S2† and Table S1†). Considering the layered structure of $\text{Bi}_9\text{O}_{7.5}\text{S}_6$ (see Fig. S3†), the pressure-induced structure deformation will mainly take place in the interlayer due to the weak interaction of van der Waals force. From the side and top views of 2D-type and 3D-type structures at ambient

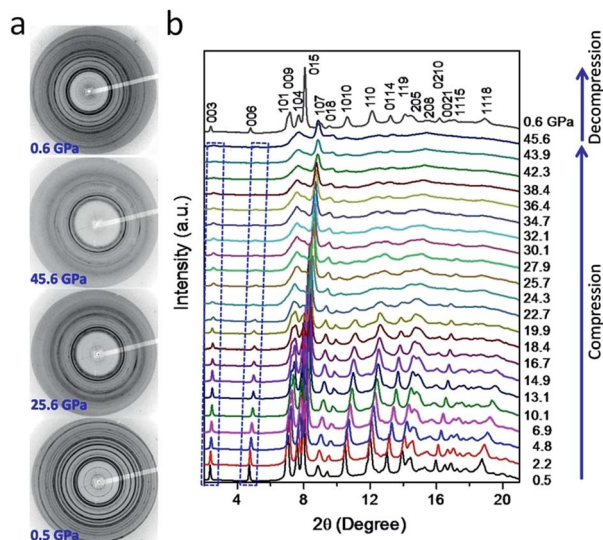


Fig. 1 Selected synchrotron XRD patterns of $\text{Bi}_9\text{O}_{7.5}\text{S}_6$ during compression up to 45.6 GPa and decompression. (a) The raw 2D XRD patterns and (b) integrated 1D profiles. The XRD pattern after decompression can be indexed with the same crystal structure (space group $R\bar{3}m$) of the pristine materials.

pressure and 22.7 GPa (Fig. 2), a tiny difference in $\text{Bi}_9\text{O}_{7.5}\text{S}_6$ structure can be realized by systematically shifting O atoms in the Bi_2O_2 layers, resulting in the decrease of the interlayer spacing. The detailed structural evolution will be discussed later.

Fig. 3 shows the *in situ* optical microphotographs of single-crystal $\text{Bi}_9\text{O}_{7.5}\text{S}_6$ in DAC during compression and after decompression. Below 23.5 GPa, the single-crystal sample remained a hexagonal plate-like morphology with a good transparency. Above 23.5 GPa, the sample became completely non-transparent and possessed a little larger top surface than the initial one. The change of transparency can be attributed to the polycrystalline transition driven by high pressure confirmed by TEM studies. From HRTEM micrographs (Fig. S4†), three well-

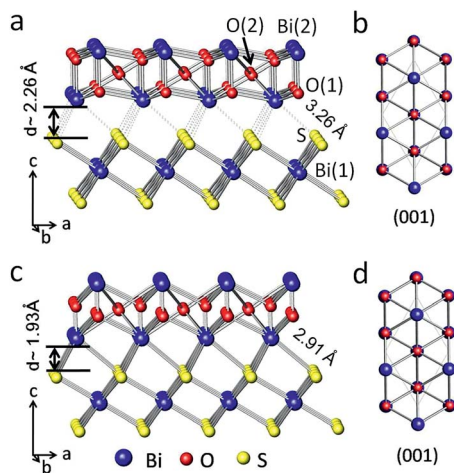


Fig. 2 The side view (projected on ac plane) and top view (projected on ab plane) of $R\bar{3}m$ structure in $\text{Bi}_9\text{O}_{7.5}\text{S}_6$ at ambient pressure (a and b) and 22.7 GPa (c and d). The dashed lines show the nominal Bi–S bonds at ambient pressure.

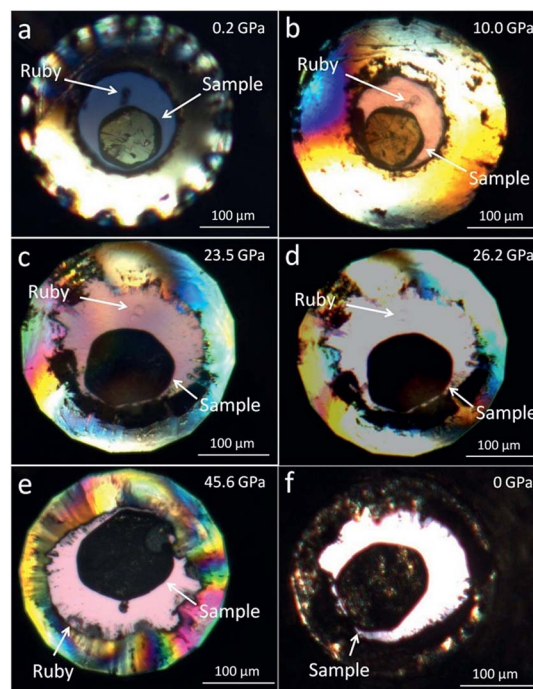


Fig. 3 The optical microphotographs of single-crystal $\text{Bi}_9\text{O}_{7.5}\text{S}_6$ in DAC during compression up to 45.6 GPa and after decompression.

resolved crystallographic planes (009), (110) and (101) can be observed in both samples, which indicate the phase stabilization after decompression corresponding to the XRD results. From the SAED images (inset of Fig. S4†), it was clearly revealed that all diffraction points can be well indexed with the structural model obtained from the XRD data. However, after the pressure treatment, the diffraction points tend to be dispersed, indicating the polycrystalline nature of the sample. The morphology and elemental distribution of the sample before and after high-pressure treatment were also checked by SEM (Fig. S5†). The polyhedral morphology of the sample can be maintained after decompression. EDS mapping analysis of selected regions showed a uniform composition distribution for both samples.

As a result of the co-action of the carrier concentration and the carrier mobility, electronic transport property is one of the critical factors for photovoltaic materials.^{36,37} To explore the pressure-induced conductivity evolution of $\text{Bi}_9\text{O}_{7.5}\text{S}_6$, we performed *in situ* resistance measurements in a DAC device during the compression and decompression (shown as insert in Fig. 4). The Van der Pauw method³² was adopted for the resistance determination with the equation, $\exp(-\pi R_1/R_S) + \exp(-\pi R_2/R_S) = 1$, where R_1 and R_2 are the two resistances measured by the four-probe method and R_S is the sample resistance. Fig. 4 shows the resistance evolutions of $\text{Bi}_9\text{O}_{7.5}\text{S}_6$ as a function of pressure. With increasing pressure, the resistance of the sample shows a rapid decrease till 10.5 GPa and then reach a shoulder peak at 22.1 GPa, followed by a fast drop up to 58.1 GPa. Definitely, the crystal and electronic structures tuned by pressure could result in the resistance change, as demonstrated in previous high pressure studies.^{20,22} The first sharp decreasing of resistance below 10.5 GPa can be attributed to the broadening of the

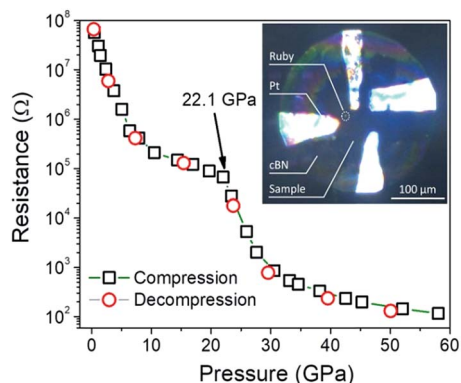


Fig. 4 Pressure-dependent electrical resistance of $\text{Bi}_9\text{O}_{7.5}\text{S}_6$ during compression and decompression (the inset displays microphotograph of the sample in DAC with Pt probes).

valence and conduction bands which caused by the shortening and bending of bonds.^{38,39} As confirmed by the synchrotron XRD results, there is no structural symmetry change detected in $\text{Bi}_9\text{O}_{7.5}\text{S}_6$ under high pressure up to 45.6 GPa. Thus, the resistance decreases gently above 10.5 GPa and shows a shoulder peak at 22.1 GPa corresponding to the evolution of the crystal structure from 2D layered structure to 3D network structure, which result in the change of electronic structure as reported in many semiconductors while without pressure-induced crystal structural transition.^{27,40} Upon further compression (>22.1 GPa), the second sharp decreasing of the resistance should be associated with a new 3D network structure generated under high pressure. The minimum resistance reaches almost 6 orders of magnitude lower than the starting value.

Considering the promoted electrical conductivity, *in situ* photocurrent measurements of $\text{Bi}_9\text{O}_{7.5}\text{S}_6$ under high pressure were conducted by using two-point-probe within DAC devices as schematically shown in Fig. 5a. The photocurrent densities (J_{ph}) of $\text{Bi}_9\text{O}_{7.5}\text{S}_6$ are given as a function of pressure in Fig. 5a. Initially, the photocurrent grows gradually with increasing pressure and can reach up to about $0.41 \mu\text{A}$ ($\sim 3.34 \text{ mA cm}^{-2}$ for 20 mW cm^{-2} illumination) at 10.5 GPa which is 4 times of that at 0.6 GPa. Above 10.5 GPa, the photocurrent decreases slowly up to 22.1 GPa, which is properly attributed to the transition of the electronic structure. Subsequently, the photocurrent increases rapidly with increasing pressure and reaches up to $7.03 \mu\text{A}$ ($\sim 58.58 \text{ mA cm}^{-2}$ for 20 mW cm^{-2} illumination) at 58.1 GPa, which is 78 times of that at 0.6 GPa and 4 orders of magnitude higher than the one reported at ambient pressure ($\sim 8 \mu\text{A cm}^{-2}$ for 100 mW cm^{-2} illumination).¹³ This significantly enhanced photocurrent is even higher than those of traditional PV materials under 100 mW cm^{-2} illumination, such as CIGS (25.7 mA cm^{-2}),⁸ CZTS (12.40 mA cm^{-2})¹⁰ and CdTe (23.26 mA cm^{-2}).¹¹ In fact, the photocurrent data were collected for several cycles of high pressure treatments. During the second compression cycle (see Fig. S6†), the photocurrent below 22.1 GPa is slightly larger than that in the first cycle, which can be ascribed to the improved density of the ceramic sample or the recrystallization effect as reported previously.¹⁹ However, above 22.1 GPa, the photocurrent is very closed to that

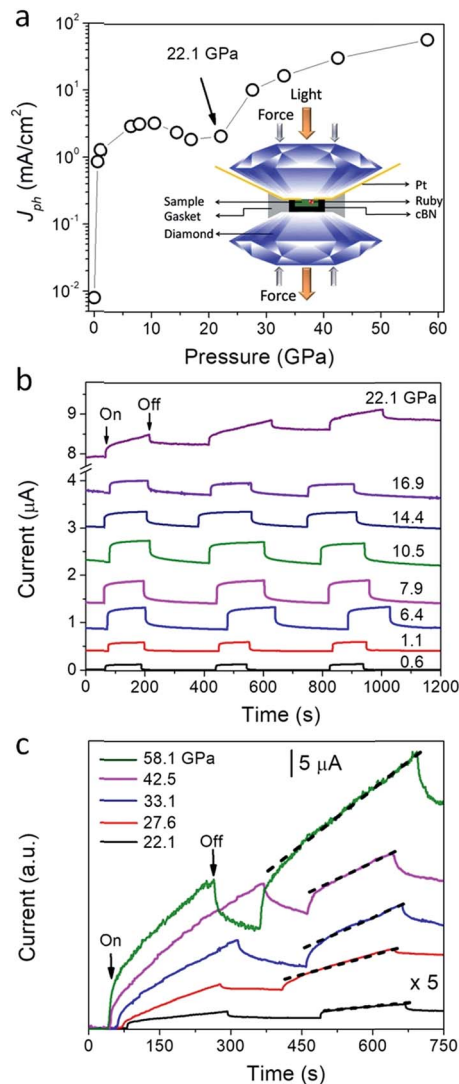


Fig. 5 (a) Photocurrent density (J_{ph}) of $\text{Bi}_9\text{O}_{7.5}\text{S}_6$ as a function of pressure (the inset shows the schematic of the high pressure DAC set up). $I-t$ characteristic of $\text{Bi}_9\text{O}_{7.5}\text{S}_6$ during compression: (b) for the region from 0.6 GPa to 22.1 GPa and (c) for the normalized current under the pressure from 22.1 GPa to 58.1 GPa. The dashed lines show the photocurrent generated in two processes.

in the first cycle, revealing a good repeatability of the photocurrent measurements. This repeatability can be also confirmed by the recovered value of J_{ph} after several decompressions (see Fig. S6†). From Fig. 5b and S7,† one can see that the dark current increases fast with increasing pressure, which is related to the pressure-induced enhancement of the conductivity. Two distinct states can be revealed in the on/off current curves under entire selected pressures. It is worth noting that two different slopes can be observed in the current curves under both on/off states starting from 22.1 GPa and more pronounced at higher pressure (see Fig. 5c), which also confirm the change of the crystal structure and electronic configuration. Under illumination, the initial sharp increase of the current could be assigned to the intrinsic photocurrent, while the subsequent gentle increase is associated with the photothermal effect that always

coexist with the photovoltaic effect.^{41,42} As marked with the dashed lines in Fig. 5c, the slope of the current inclines upward notably with increasing pressure, indicating the enhanced pressure-induced photothermal effect. Actually, high-pressure studies have been conducted on several photovoltaic materials, such as organometal halide perovskites,^{19,20} GaAs²¹ and KBiFe_2O_5 ,²² only pressure-enhanced photoelectric performance has been reported in KBiFe_2O_5 so far. Thus, the giant pressure-induced enhancement of the photocurrent in an optoelectronic material is really scarce and may offer potential applications in photovoltaic devices as switcher or controller.

The BM-EoS fitting results in Fig. 6a and normalized cell parameters *versus* pressure data in Fig. 6b, as neither of them exhibits any discontinuity, further confirm the absence of a first-order structural transition. The pressure dependent cell volume (*V*) could be well fitted to an isothermal Birch–Murnaghan equation of state (BM-EoS): $p(V) = 1.5B_0[(V_0/V)^{7/3} - (V_0/V)^{5/3}] \times \{1 + 0.75(B'_0 - 4)[(V_0/V)^{2/3} - 1]\}$, where B_0 and B'_0 are the bulk modulus and its pressure derivative, respectively.^{43,44} With unit cell volume V_0 fixed at the experimental value of 444.80 \AA^3 ,¹³ the fitting yields a bulk modulus $B_0 \sim 66.4 \pm 1.1 \text{ GPa}$ and a derivative of bulk modulus $B'_0 \sim 4.5 \pm 0.1$. At ambient conditions, the crystal structure of $\text{Bi}_9\text{O}_{7.5}\text{S}_6$ features two-dimensional (2D) hexagonal layers of $[\text{BiS}_2]$ and $[\text{Bi}_2\text{O}_2]$ alternately stacked along *c*-axis, as shown in Fig. S5.† During the initial compression, cell parameter *c* is much more compressible than *a* due to the weak van der Waals interaction between BiS_2 and Bi_2O_2 layers along *c*-axis, while higher pressure allows them to have nearly isotropic contractions (see Fig. 6b). Since (003) and (006) crystallographic planes correspond to Bi–O and Bi–S layers, respectively, such a trend is more pronounced by comparing the intensity ratios of (003)/(015) and (006/015) with a turning point at 22.7 GPa (Fig. 6c), indicating an intrinsic structure evolution driven by pressure. (015) was selected as the highest diffraction intensity. The relative intensity of (006/015) drops faster than that of (003)/(015) below 22.7 GPa, which is related to Bi–S layers under a larger distortion. To verify this statement, the comparison of the shrinkages between the Bi–O and Bi–S layers under compression has been shown in Fig. S8.† With increasing pressure, the normalized thickness of Bi–S layer decreases more rapidly than that of Bi–O layer up to 22.7 GPa, and then shows a gentle slope similar to that of Bi–O layer above 22.7 GPa. This trend is consistent with the evolution of the bond length of Bi(1)–S. Additionally, upon forming 3d network, the distinguished Bi–S layer is no more layered, leading to the isotropic contraction above 22.7 GPa.

The gradual closure of the van der Waals gap is confirmed by tracking the nominal bond length of neighboring Bi(2)–S atoms, as well as the distance, between BiS_2 and Bi_2O_2 layers (Fig. 6d). Both of these values decrease gradually with increasing pressure and show a sudden downturn above 19.9 GPa. At 22.7 GPa, the bond length of Bi(2)–S (2.91 Å) is shorter than that in $\text{Bi}_2\text{O}_2\text{S}$ (3.02 Å, one of the longest bond length reported for Bi–S⁴⁵), suggesting the formation of a three-dimensional (3D) network structure by the bonding interaction of Bi(2)–S (as shown in Fig. 6d). Since there is no notable change in Bi(1)–S layers due to the isotropic contraction, the slight

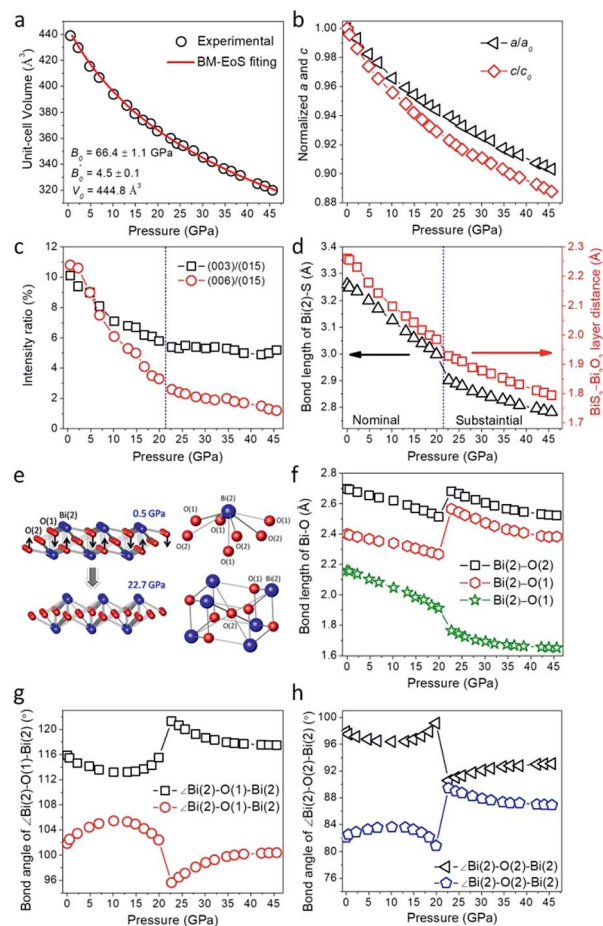


Fig. 6 (a) Unit cell volume vs. pressure and the third-order BM-EoS fitting. (b) Normalized cell parameters a/a_0 and c/c_0 versus pressure. (c) The intensity ratios of (003)/(015) and (006/015). (d) The pressure-dependent nominal bond length of neighboring Bi(2)–S atoms and the nearest distance between BiS_2 and Bi_2O_2 layers. (e) The schematic Bi–O layers at 0.5 GPa and 22.7 GPa (left), the oxygen coordination environment of Bi(2) (upper right) and hexagonal prism of Bi_6O_6 (lower right). The black arrows indicate the sliding path for the O(1) atoms under high pressure. The bond length of Bi(2)–O (f) and the bond angles of $\angle \text{Bi(2)–O(1)–Bi(2)}$ (g) and $\angle \text{Bi(2)–O(2)–Bi(2)}$ (h) at varied pressures.

difference in crystal structure induced by high pressure mainly originate from the Bi(2)–O layers. The sketch map of the Bi(2)–O layer is shown in Fig. 6e. The oxygen coordination number of Bi(2) is seven, with four O(1) atoms and three half-occupied O(2) atoms. Six O(1) atoms and six Bi(2) atoms construct a distorted hexagonal prism with a half-occupied O(2) atom located in the center. As illustrated in Fig. 6e, one sliding path for O atoms was proposed by the black arrows mainly due to the enhanced electrostatic repulsive of S atoms driven by high pressure, which finally results in the structural evolution from 2D to 3D model. The scenario of the formation of Bi(2)–S bond can be also confirmed by the evolutions of the bond lengths of Bi(2)–O (Fig. 6f) and Bi(1)–S (Fig. S8†), as well as the bond angles of $\angle \text{Bi(2)–O–Bi(2)}$ (Fig. 6g and h) and $\angle \text{S–Bi(1)–S}$ (Fig. S8†) under high pressure. Above 22.7 GPa, a sudden change can be apparently observed in all of them, corresponding to the bonding interaction of Bi(2)–S.

Actually, it has been demonstrated that hydrostatic pressure can greatly affect the physical/chemical properties of functional materials, including the bandgap adjustment.^{17,20–22} To detect the pressure effects on the band gap of $\text{Bi}_9\text{O}_{7.5}\text{S}_6$, *in situ* PL measurements on a single crystal under hydrostatic pressure up to 32.8 GPa were carried out in a DAC (the microphotographs of the sample in DAC were shown in Fig. S9†). At ambient pressure, two distinct PL emission peaks were found in single-crystal $\text{Bi}_9\text{O}_{7.5}\text{S}_6$, one is the near band edge emission at 1.34 eV (926 nm) close to the previously reported E_0 (1.27 eV) by Meng *et al.*,¹³ and the other shoulder peak at around 1.53 eV (812 nm) should be attributed to the defect related emission as also observed in other oxygen-deficient systems such as ZnO ,⁴⁶ TiO_2 (ref. 47) and P_xO_y .⁴⁸ As shown in Fig. 7a, the band gap can be extracted from the PL peaks under pressure by fitting them with Gaussian functions. The PL peak positions show a gradual red shift and the fluorescence intensity decreases upon compression, which confirms the closing of the bandgap. Above 10 GPa, the PL peaks are hard to be detected. Actually, the distances of adjacent atoms should be reduced by pressurization, which leads to enhanced possibility of electronic orbital overlapping, spin flipping, spin-orbital coupling, intersystem crossing, *etc.* Thus, the pressurization-induced fluorescence quenching will take place due to the activation energy transfer and excimer/exciple formation, as extensively reported in other chalcogenides and arsenides.^{21,49,50} After decompression, the PL peak recovered back to 930 nm as the restoration of the ambient crystalline structure. The reduction of the bandgap was also confirmed by first-principles calculations using the structure model refined from high-pressure XRD data. As shown in Fig. 7b, the calculated theoretical bandgaps up to 10 GPa are almost identical to the value obtained from PL spectra. The bandgap E_g decreased sharply from ambient pressure to 23 GPa followed by a gentle decreasing to the highest pressure of 45 GPa, corresponding to the structural evolution from 2D to 3D phase. The electronic band structure reveals the semiconductor nature of $\text{Bi}_9\text{O}_{7.5}\text{S}_6$

with a direct-transition band gap below 10 GPa. However, the relative energy positions of valence and conduction bands between Γ and A points are almost identical at 15 GPa (Fig. 7c) and tend to be interlaced at higher pressures (Fig. S10†), suggesting the crossover from direct- to indirect bandgap transition which properly leads to the decreasing in PL intensity under pressure. According to the partial density of state (PDOS) analyses shown in Fig. 7d, the valence band (VB) consists of Bi 6s, S 3p, and O 2p orbitals, while the conduction band (CB) is mainly contributed by Bi 6p orbital. Thus, the bandgap closing induced by pressure should be mainly attributed to the shrinkage of $[\text{BiS}_2]$ and $[\text{Bi}_2\text{O}_2]$ hexagonal layers.

4. Conclusions

In summary, the structural stability, electrical conductivity and visible-light response have been studied in layered bismuth oxysulfide $\text{Bi}_9\text{O}_{7.5}\text{S}_6$ as a function of hydrostatic pressures up to 58.1 GPa at room temperature. *In situ* synchrotron X-ray diffraction studies revealed the $R\bar{3}m$ structure evolved from 2D layered structure to 3D networked structure without symmetry breaking under pressure, which is mainly associated with the shrinkage of Bi_2O_2 polyhedral layers. The *in situ* electrical conductivity and photocurrent measurements show that pressure can significantly affect not only the crystal structure but also the photoelectric related properties. In particular, the giant enhancement of electrical conductivity and photoelectric response can be realized under high pressure, suggesting that the pressure-induced structural evolution may offer potential applications in photovoltaic devices as switcher or controller and explore new materials with improved photovoltaic performance.

Conflicts of interest

There are no conflicts to declare.

Acknowledgements

This work was financially supported by NSAF under Grant No. U1530402. HPCAT operations are supported by DOE-NNSA under Award No. DE-NA0001974 and DOE-BES under Award No. DE-FG02-99ER45775, with partial instrumentation funding by NSF. APS is supported by DOE-BES, under Contract No. DE-AC02-06CH11357. G. Z. acknowledges financial support from NSFC under Grant No. 51772184.

Notes and references

- 1 Y. Mizuguchi, H. Fujihisa, Y. Gotoh, K. Suzuki, H. Usui, K. Kuroki, S. Demura, Y. Takano, H. Izawa and O. Miura, *Phys. Rev. B: Condens. Matter Mater. Phys.*, 2012, **86**, 220510.
- 2 S. K. Singh, A. Kumar, B. Gahtori, G. Sharma, S. Patnaik and V. P. S. Awana, *J. Am. Chem. Soc.*, 2012, **134**, 16504–16507.
- 3 W. A. Phelan, D. C. Wallace, K. E. Arpino, J. R. Neilson, K. J. Livi, C. R. Seabourne, A. J. Scott and T. M. McQueen, *J. Am. Chem. Soc.*, 2013, **135**, 5372–5374.

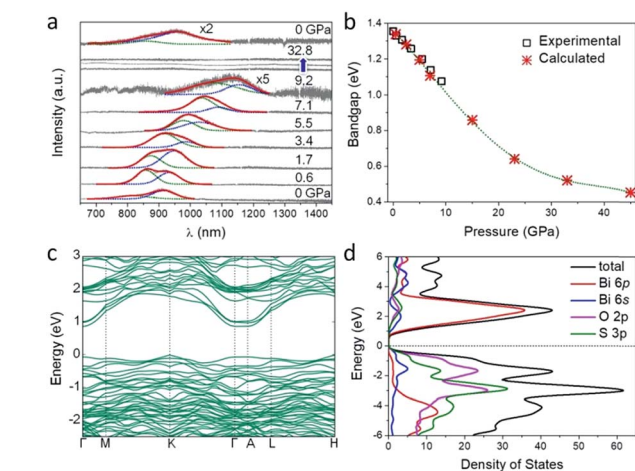


Fig. 7 Pressure-dependent PL spectra (a) and bandgaps (b) derived from PL of $\text{Bi}_9\text{O}_{7.5}\text{S}_6$ during compression and decompression. A 325 nm laser with 3 mW power was used for irradiation. Electronic band structure (c) and calculated density of states from each element (d) of $\text{Bi}_9\text{O}_{7.5}\text{S}_6$ at 15 GPa.

- 4 G. Ren, S. Wang, Y. Zhu, K. J. Ventura, X. Tan, W. Xu, Y. Lin, J. Yang and C. Nan, *Energy Environ. Sci.*, 2017, **10**, 1590–1599.
- 5 S. D. N. Luu and P. Vaqueiro, *J. Mater. Chem. A*, 2013, **1**, 12270–12275.
- 6 J. Wu, H. Yuan, M. Meng, C. Chen, Y. Sun, Z. Chen, W. Dang, C. Tan, Y. Liu, J. Yin, Y. Zhou, S. Huang, H. Q. Xu, Y. Cui, H. Y. Hwang, Z. Liu, Y. Chen, B. Yan and H. Peng, *Nat. Nanotechnol.*, 2017, **12**, 530–534.
- 7 J. Wu, Y. Liu, Z. Tan, C. Tan, J. Yin, T. Li, T. Tu and H. Peng, *Adv. Mater.*, 2017, **29**, 1704060.
- 8 D. B. Mitzi, M. Yuan, W. Liu, A. J. Kellock, S. J. Chey, V. Deline and A. G. Schrott, *Adv. Mater.*, 2008, **20**, 3657–3662.
- 9 A. Gavriluta, T. Fix, A. Nonat, A. Slaoui, J. Guillemoles and L. J. Charbonnière, *J. Mater. Chem. A*, 2017, **5**, 14031–14040.
- 10 J. B. Li, V. Chawla and B. M. Clemens, *Adv. Mater.*, 2012, **24**, 720–723.
- 11 J. D. Major, R. E. Treharne, L. J. Phillips and K. Durose, *Nature*, 2014, **511**, 334–337.
- 12 X. Zhang, Y. Liu, G. Zhang, Y. Wang, H. Zhang and F. Huang, *ACS Appl. Mater. Interfaces*, 2015, **7**, 4442–4448.
- 13 S. Meng, X. Zhang, G. Zhang, Y. Wang, H. Zhang and F. Huang, *Inorg. Chem.*, 2015, **54**, 5768–5773.
- 14 T. L. Bahers, S. Haller, T. L. Mercier and P. Barboux, *J. Phys. Chem. C*, 2015, **119**, 17585–17595.
- 15 W. Yang, X. Huang, R. Harder, J. N. Clark, I. K. Robinson and H. K. Mao, *Nat. Commun.*, 2013, **4**, 1680.
- 16 C. Xu, W. Xiao, T. Liu, F. Sun, J. Zheng, S. Peng, X. Liu, F. Pan, W. Yang and H. Mao, *J. Mater. Chem. A*, 2017, **5**, 19390–19397.
- 17 Y. Cao, G. Qi, C. Liu, L. Wang, Z. Ma, K. Wang, F. Du, G. Xiao and B. Zou, *J. Phys. Chem. C*, 2018, **122**, 9332–9338.
- 18 G. Xiao, Y. Cao, G. Qi, L. Wang, C. Liu, Z. Ma, X. Yang, Y. Sui, W. Zheng and B. Zou, *J. Am. Chem. Soc.*, 2017, **139**, 10087–10094.
- 19 X. Lü, Y. Wang, C. C. Stoumpos, Q. Hu, X. Guo, H. Chen, L. Yang, J. S. Smith, W. Yang, Y. Zhao, H. Xu, M. G. Kanatzidis and Q. Jia, *Adv. Mater.*, 2016, **28**, 8663–8668.
- 20 Y. Wang, X. Lü, W. Yang, T. Wen, L. Yang, X. Ren, L. Wang, Z. Lin and Y. Zhao, *J. Am. Chem. Soc.*, 2015, **137**, 11144–11149.
- 21 I. Zardo, S. Yazji, C. Marini, E. Uccelli, A. F. Morral, G. Abstreiter and P. Postorino, *ACS Nano*, 2012, **6**, 3284–3291.
- 22 G. Zhang, F. Liu, T. Gu, Y. Zhao, N. Li, W. Yang and S. Feng, *Adv. Electron. Mater.*, 2017, **3**, 1600498.
- 23 G. Xiao, Y. Wang, D. Han, K. Li, X. Feng, P. Lv, K. Wang, L. Liu, S. A. T. Redfern and B. Zou, *J. Am. Chem. Soc.*, 2018, **140**, 13970–13975.
- 24 Z. Ma, Z. Liu, S. Lu, L. Wang, X. Feng, D. Yang, K. Wang, G. Xiao, L. Zhang, S. A. T. Redfern and B. Zou, *Nat. Commun.*, 2018, **9**, 4506.
- 25 W. S. Zheng, T. Xie, Y. Zhou, Y. L. Chen, W. Jiang, S. L. Zhao, J. X. Wu, Y. M. Jing, Y. Wu, G. C. Chen, Y. F. Guo, J. B. Yin, S. Y. Huang, H. Q. Xu, Z. F. Liu and H. L. Peng, *Nat. Commun.*, 2015, **6**, 6972.
- 26 M. Mazur, A. M. Arévalo-López, P. S. Wheatley, G. P. M. Bignami, S. E. Ashbrook, Á. Morales-García, P. Nachtigall, J. P. Attfield, J. Čejka and R. E. Morris, *J. Mater. Chem. A*, 2018, **6**, 5255–5259.
- 27 Z. Zhao, H. Zhang, H. Yuan, S. Wang, Y. Lin, Q. Zeng, G. Xu, Z. Liu, G. K. Solanki, K. D. Patel, Y. Cui, H. Y. Hwang and W. L. Mao, *Nat. Commun.*, 2015, **6**, 7312.
- 28 L. Zhu, H. Wang, Y. Wang, J. Lv, Y. Ma, Q. Cui, Y. Ma and G. Zou, *Phys. Rev. Lett.*, 2011, **106**, 145501.
- 29 H. K. Mao, J. Xu and P. M. J. Bell, *J. Geophys. Res.*, 1986, **91**, 4673–4676.
- 30 A. P. Hammersley, S. O. Svensson, M. Hanfland, A. N. Fitch and D. Hausermann, *High Pressure Res.*, 1996, **14**, 235–248.
- 31 A. C. Larson and R. B. Von Dreele, *General Structure Analysis System (GSAS)*, Los Alamos National Laboratory Report, LAUR, 2000, p. 86.
- 32 L. J. van der Pauw, *Philips Res. Rep.*, 1958, **13**, 1–9.
- 33 P. E. Blöchl, *Phys. Rev. B: Condens. Matter Mater. Phys.*, 1994, **50**, 17953.
- 34 J. P. Perdew, K. Burke and M. Ernzerhof, *Phys. Rev. Lett.*, 1996, **77**, 3865.
- 35 H. J. Monkhorst and J. D. Pack, *Phys. Rev. B: Condens. Matter Mater. Phys.*, 1976, **13**, 5188.
- 36 G. Zhang, H. Wu, G. Li, Q. Huang, C. Yang, F. Huang, F. Liao and J. Lin, *Sci. Rep.*, 2013, **3**, 1265.
- 37 M. Tuteja, A. B. Mei, V. Palekis, A. Hall, S. MacLaren, C. S. Ferekides and A. A. Rockett, *J. Phys. Chem. Lett.*, 2016, **7**, 4962–4967.
- 38 Y. Ma, M. Eremets, A. R. Oganov, Y. Xie, I. Trojan, S. Medvedev, A. O. Lyakhov, M. Valle and V. Prakapenka, *Nature*, 2009, **458**, 182–185.
- 39 K. Arai, K. Kumata, K. Kadota, K. Yamamoto, H. Namikawa and S. Saito, *J. Non-Cryst. Solids*, 1973, **13**, 131–139.
- 40 Y. Wang, Z. Zhou, T. Wen, Y. Zhou, N. Li, F. Han, Y. Xiao, P. Chow, J. Sun, M. Pravica, A. L. Cornelius, W. Yang and Y. Zhao, *J. Am. Chem. Soc.*, 2016, **138**, 15751–15757.
- 41 M. Barkelid and V. Zwiller, *Nat. Photonics*, 2014, **8**, 47–51.
- 42 P. V. Kamet, *Nat. Chem.*, 2010, **2**, 809–810.
- 43 F. Birch, *Phys. Rev.*, 1947, **71**, 809.
- 44 F. D. Murnaghan, *Proc. Natl. Acad. Sci. U. S. A.*, 1944, **30**, 244–247.
- 45 E. Koyama, I. Nakai and K. Nagashima, *Acta Crystallogr., Sect. B: Struct. Sci.*, 1984, **40**, 105–109.
- 46 X. L. Wu, G. G. Siu, C. L. Fu and H. C. Ong, *Appl. Phys. Lett.*, 2001, **78**, 2285–2287.
- 47 Y. Lei, L. D. Zhang, G. W. Meng, G. H. Li, X. Y. Zhang, C. H. Liang, W. Chen and S. X. Wang, *Appl. Phys. Lett.*, 2001, **78**, 1125.
- 48 J. Pei, X. Gai, J. Yang, X. Wang, Z. Yu, D. Choi, B. Luther-Davies and Y. Lu, *Nat. Commun.*, 2016, **7**, 10450.
- 49 U. Venkateswaran, M. Chandrasekhar, H. R. Chandrasekhar, B. A. Vojak, F. A. Chambers and J. M. Meese, *Phys. Rev. B: Condens. Matter Mater. Phys.*, 1986, **33**, 8416–8423.
- 50 F. Li, Y. Yan, B. Han, L. Li, X. Huang, M. Yao, Y. Gong, X. Jin, B. Liu, C. Zhu, Q. Zhou and T. Cui, *Nanoscale*, 2015, **7**, 9075–9082.